RSC Advances

ROYAL SOCIETY OF CHEMISTRY

www.rsc.org/advances

$LaCoO_3$–based sensors, as fabricated of $LaCoO_3$ nanoparticles of ~82 nm, show a response of ~279.86 toward CO at 500 °C, due to the high content of O_2^{2-}/O^- species in $LaCoO_3$.

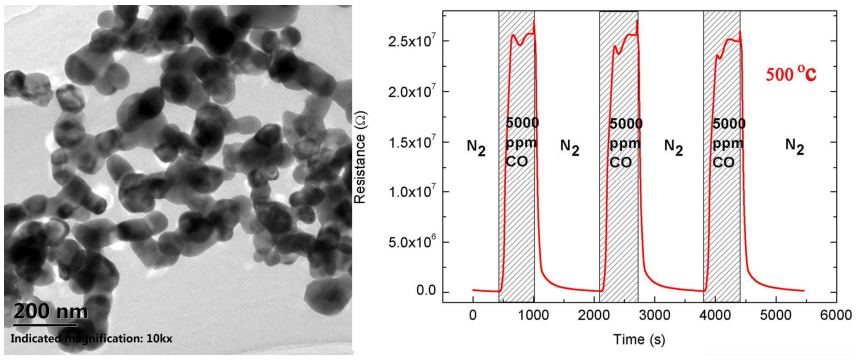

RSC Advances

PAPER

$LaCoO_3$–based sensors with high sensitivity to carbon monoxide

Jun-Chao Ding, Hua-Yao Li, Ze-Xing Cai, Xiao-Dong Zhang, Xin Guo*

Received 00th January 20xx,
Accepted 00th January 20xx

DOI: 10.1039/x0xx00000x

www.rsc.org/

$LaCoO_3$ nanoparticles with particle size of ~82 nm was prepared by co-precipitation, and mesoporous $LaCoO_3$ thick films with a thickness of ~7 μm were fabricated by screen printing the nanoparticles on Al_2O_3 substrates. The CO sensing properties of the $LaCoO_3$ thick films were characterized in the temperature range of 100 to 550 °C. Under 5000 ppm CO at 500 °C, the thick film sensor achieved a high sensing response of ~279.86, with response and recovery periods of 181 and 311 s, respectively. Under 25 ppm CO at 500 °C, a reasonable response of 1.04 was also achieved. Moreover, the sensor demonstrated reliable dynamic response-and-recovery at a temperature as low as 100 °C, therefore, $LaCoO_3$ is very promising for CO sensing at low temperatures. The high response to CO could be ascribed to the high content of O_2^{2-}/O^- species in $LaCoO_3$.

1. Introduction

Carbon monoxide (CO) is a well-known poisonous gas able to attack hemoglobin from the blood, preventing the supply of needed oxygen to different parts of human body.[1] Early detection of CO is therefore essential to prevent health hazards. Rare earth transition metal oxides with a perovskite structure have been used as catalysts for various chemical reactions, including CO oxidation.[2-4] Among these oxides, $LaCoO_3$ and the related compounds have attracted special attention due to their excellent catalytic performance in the oxidation of CO.[5,6] Therefore, $LaCoO_3$ is very promising for having excellent CO sensing performance. $LaCoO_3$ is a p-type conductor with a rhombohedrally-distorted perovskite structure, and the electronic conduction occurs through the transfer of charge carriers *via* Co–O–Co bonds.[7,8]

Several synthesis methods for the preparation of $LaCoO_3$, including solid-state reaction,[9] sol–gel method,[10] co-precipitation,[11] combustion method,[12] spray-freezing/freeze-drying,[13] flame-spray pyrolysis,[14] *etc*., have been developed. Among them the benchmark method is solid-state reaction. Generally, the $LaCoO_3$ particles prepared via solid-state reaction at high temperatures (above 1000 °C) often have relatively large particle size and easily form coarse aggregation.[15] Large-sized or aggregated particles often result in low surface activity per unit mass, thus yielding low gas sensing properties. Recently, gas sensors fabricated from nanoparticles have caught significant attentions, due to their advantages of high sensitivity and low operating temperature.[16] Excellent gas sensing properties have been demonstrated for the nanoparticles of numerous oxides, including SnO_2,[17] ZnO,[18] WO_3[19] and TiO_2.[20] The enhanced gas sensing properties of nanoparticles comparing to bulk sample can be attributed to the increased surface-to-volume ratio of the nanoparticles, which leads to the adsorption of more reactant species.[21]

In the present work, $LaCoO_3$ nanoparticles were prepared by co-precipitation, and $LaCoO_3$ thick films were fabricated by screen printing the nanoparticles on Al_2O_3 substrates. The $LaCoO_3$ thick films displayed a high response of 279.86 at 500 °C, such a response is significantly higher than those of most CO sensors; and a reliable dynamic curve of response-and-recovery was obtained at a temperature as low as 100 °C, demonstrating that the sensor based on $LaCoO_3$ thick film is very promising for CO sensing at low temperatures.

2. Experimental

2.1 Sensor fabrication

A chemical co-precipitation method was used to prepare $LaCoO_3$ nanoparticles. $Co(NO_3)_2{\cdot}6H_2O$ (Analytical reagent (AR), Sinopharm) and $La(NO_3)_3{\cdot}nH_2O$ (AR, Sinopharm) were weighted according to a nominal molar ratio of Co/La = 1, and then dissolved in deionized water. H_2O_2 (AR, Sinopharm) (equimolar with respect to Co(II)) was then added to oxidize Co(II) to Co(III). Afterwards, NaOH (AR, Sinopharm) solution was added to adjust the pH value to 11 ~ 12. The resulted precipitate was rinsed with deionized water until pH = 7, and then dried at 80 °C for 2 h. The rinsing process involved several cycles of centrifugation/washing/re-dispersion. Finally, $LaCoO_3$ nanoparticles were obtained by calcination at 650 °C for 6 h in air.

Screen printing technique was used to fabricate thick-film type sensors. First, 70 wt.% of $LaCoO_3$ nanoparticles were mixed with 30 wt.% of organic vehicle composing of terpineol (CP, Aldrich), diethylene glycol monobutyl ether acetate (98%,

Laboratory of Solid State Ionics, School of Materials Science and Engineering, Huazhong University of Science and Technology, Wuhan 430074, P.R. China. E-mail: xguo@hust.edu.cn

Aldrich) and dibutyl phthalate (98.5%, Aldrich). The mixture was then ground in a mortar for 2 h to obtain the printing paste. The paste was screen-printed on Al_2O_3 substrates, and then calcined at 800°C for 2h to obtain $LaCoO_3$ thick films (area 14×5 mm^2). Four 2-mm-wide platinum electrodes were screen-printed on the Al_2O_3 substrate in a similar way, followed with calcination at 850 °C for 2 h in air. The electrodes were separated from each other by a space of ~4 mm.

2.2 Characterization

The crystal structure of the $LaCoO_3$ nanoparticles was determined by X-ray diffraction (XRD) (SHIMADZU XRD-7000S) in the 2θ range of 20 - 90°, operating at 40 kV and 30 mA with Cu/Kα radiation. The morphology of the $LaCoO_3$ nanoparticles was observed by transmission electron microscope (TEM, JEOL JEM-2100F). The microstructure and the element distribution of the $LaCoO_3$ films was analyzed using scanning electron microscope (SEM, JEOL JSM-7600F) equipped with an energy dispersive X-ray spectroscope (EDS). Micro-Raman spectroscopy investigations were carried out using a Confocal Raman system (JOBIN YVON, HR800) at room temperature. X-ray photoelectron spectra (XPS) were recorded with an SECA Lab2200i-XL spectrometer by using an unmonochromated Al Kα (1486.6 eV) X-ray source.

2.3 Sensing Performance

The sensor resistance was measured with the four-probe method to eliminate the contact resistance of the electrodes on the $LaCoO_3$ film, and the data were collected automatically every second using an Agilent B2901A Source Measurement Unit (SMU). A flow system was used to introduce gases with specified concentrations of CO in N_2 into the sample chamber. In this system, CO was mixed with the carrier gas (N_2) in a gas distributing system to obtain the desired CO concentrations, and the CO concentration was monitored by an Agilent 7890A Gas Chromatography System. The CO/N_2 mixed gases were introduced into the sample chamber at a flow rate of 100 SCCM. The flow rate was controlled by Mass Flow Controller (MFC) (BEIJING SEVENSTAR ELECTRONICS). A thermocouple was placed close to the sample surface to accurately monitor the sensor temperature.

3. Results and discussion

According to the XRD pattern shown in Fig. 1, the $LaCoO_3$ nanoparticles prepared by the co-precipitation method have the rhombohedral structure. Fig. 2 (a) shows the TEM image of the $LaCoO_3$ nanoparticles; the particle diameters (determined from the electron micrographs) are mostly circa 82 nm. High-resolution TEM image (Fig. 2 (b)) exhibits clear lattice fringes, most of which have distances of d = 0.269 ± 0.01 nm, corresponding to the (104)-spacing of the $LaCoO_3$ rhombohedral structure. The selected area electron diffraction (SAED) pattern (inset of Fig. 2 (b)) indicates the rhombohedral structure as well, corroborating the XRD analysis.

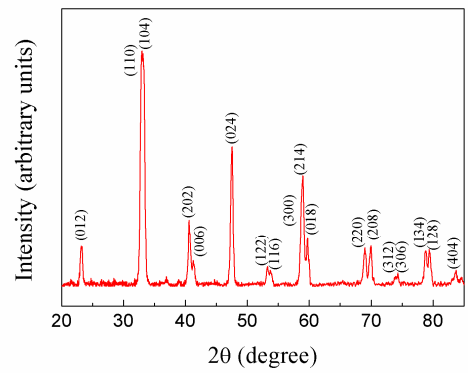

Fig. 1. XRD pattern of co-precipitated $LaCoO_3$ powder.

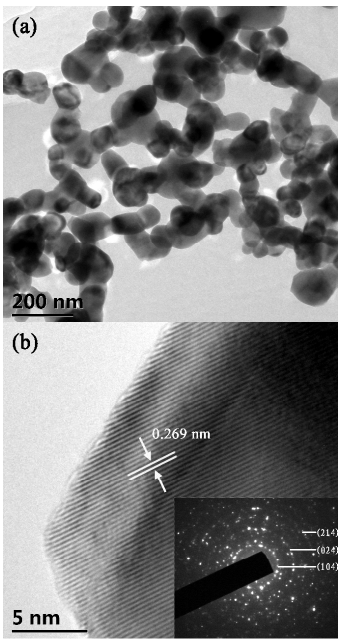

Fig. 2. (a) TEM and (b) HRTEM micrographs of co-precipitated $LaCoO_3$ nanoparticles. The inset is the electron diffraction pattern.

SEM micrographs of the $LaCoO_3$ thick film are shown in Fig. 3. The $LaCoO_3$ film is highly porous, which is preferred for gas-sensing applications. A clear boundary exists between the $LaCoO_3$ layer and the Al_2O_3 substrate, as indicated by Fig. 3 (b). Good adhesion between the sensing layer and the substrate is also obvious, and the film thickness can be determined to be ~7 μm. The EDS composition scan demonstrates no elemental inter-diffusion between the $LaCoO_3$ layer and the Al_2O_3 substrate after calcination.

The micro-Raman spectrum of the $LaCoO_3$ thick film is shown in Fig. 4. A total of ten major features can be observed at different wave number positions of 86, 130, 172, 202, 261, 380, 490, 544, 675 and 750 cm^{-1}. The feature at 261 cm^{-1} can be assigned to the A_{1g} rotational mode of O atoms around the

c axis, the one at 86 cm^{-1} can be ascribed to the E_g rotational mode of O atoms around the *a* and *b* axes, and the one at 172 cm^{-1} is due to the E_g vibrational mode of La atoms along the *a* and *b* axes.[22] The feature at 432 cm^{-1} due to the E_g bending mode and the feature at 584 cm^{-1} due to the E_g quadrupole mode cannot be observed, because the intensity of the two peaks decreases rapidly above 40 K.[22] Tang *et al*. observed a sharp feature at ca. 650 cm^{-1} in the Raman spectra of different cobalt containing compounds such as CoOOH, Co_3O_4 and CoO.[23] Thus it is likely that the feature at 675 cm^{-1} is associated with Co–O species. The feature at 544 cm^{-1} is associated with the semiconducting state of $LaCoO_3$.[24] In addition, Iliev,[25] Seikeh[26] and Li[27] reported the Raman spectra of rhombohedral $LaMnO_3$ samples showing peaks at ~490, ~380, ~130, ~202 and ~750 cm^{-1}, which is quite similar to this work. Therefore, an orthorhombic structure could be identified for the $LaCoO_3$ thick film, confirming the XRD analysis as well.

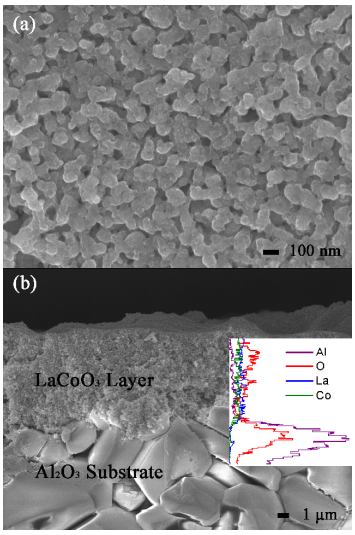

Fig. 3. SEM micrographs of $LaCoO_3$ thick film sensors (a: surface, b: cross-section).

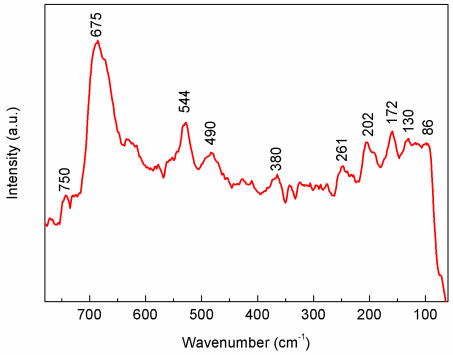

Fig. 4. Micro-Raman spectrum of $LaCoO_3$ film.

Fig. 5 shows the sensor resistance variation under alternating cycles of 5000 ppm CO and N_2 at 500 °C. The sensor resistance increases abruptly after 5000 ppm CO is introduced, and it recovers immediately when N_2 is introduced. This result indicates that the CO sensing behavior of the $LaCoO_3$ sensor is fully reversible. The sensitivity is characterized by the sensor response, which is defined as: $S = R_{CO}/R_{N2}$, in which R_{CO} is the sensor resistance in the presence of CO and R_{N2} is the resistance in N_2. At 500 °C, an extremely high response of about 279.86 is achieved. This result is significantly better than the response of SnO_2 sensors to 5000 ppm CO at 450 °C, which is about 40.[28] The response time is characterized by t_{90}, which is defined as the time gap between the onset of resistance change and the attainment of 90% relative change in resistance.[29] The t_{90} for the sensor response and recovery shown in Fig.5 are determined to be 164 and 111 *s*, respectively. Despite of the more-than-two-orders-of-magnitude change in resistance, the response and recovery are still pretty fast. Furthermore, good repeatability is achieved among individual cycles.

Fig. 6 is the response curve of the $LaCoO_3$ sensor to different CO concentrations ranging from 0 to 250 ppm at 500 °C. The sensor resistance continuously increases with rising CO concentration. Due to the limitation of the experimental setup, the lowest CO concentration is limited to 25 ppm. And as shown in the inset, the resistance has an almost perfect linear correlation with the CO concentration, which is very advantageous for the sensor calibration.

To better demonstrate the sensing property for low CO concentrations, the sensor resistance variation under alternating cycles of 25 ppm CO and N_2 at 500 °C is presented in Fig. 7. Similarly, the sensor resistance increases rapidly after 25 ppm CO is introduced and recovers immediately when CO is cut off. The response is about 1.04. This response is better than that (~1.00 after conversion the response value to the same definition) reported for SnO_2 thick-film sensors.[30] And the t_{90} for response and recovery are 868 and 302 *s*, respectively.

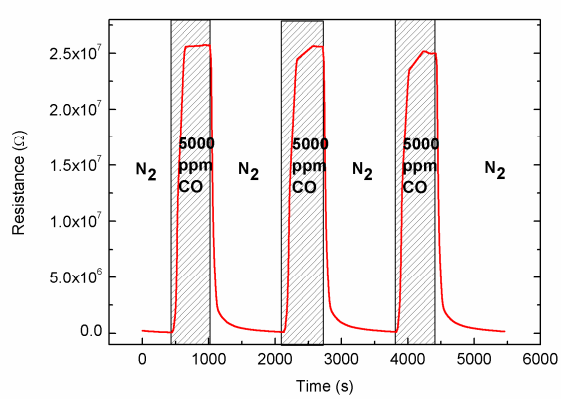

Fig. 5. Sensor resistance under alternating cycles of 5000 ppm CO and N_2 at 500 °C.

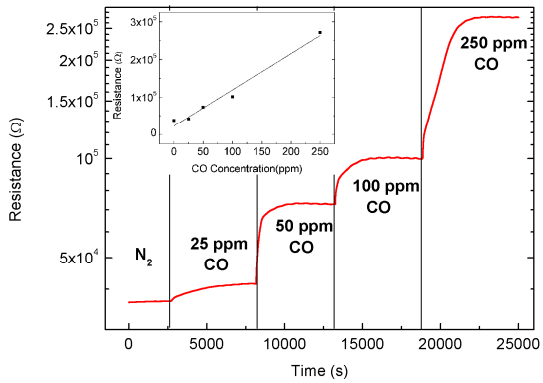

Fig. 6. Sensor resistance variation with increasing CO concentrations (0, 25, 50, 100 and 250 ppm) at 500 °C.

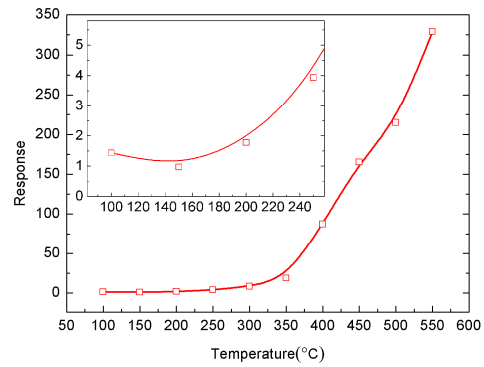

Fig. 8. Sensor response in the temperature range of 100 °C to 550 °C under 10^4 ppm CO.

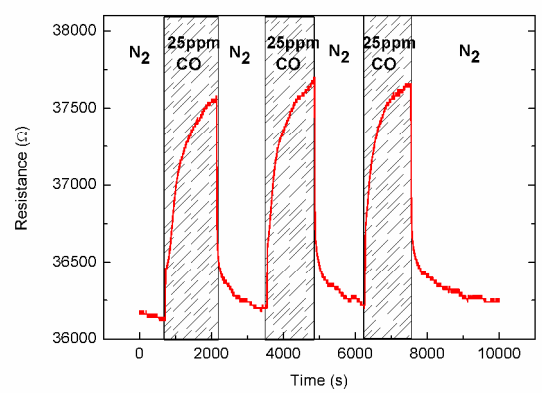

Fig. 7. Sensor resistance under alternating cycles of 25 ppm CO and N_2 at 500 °C.

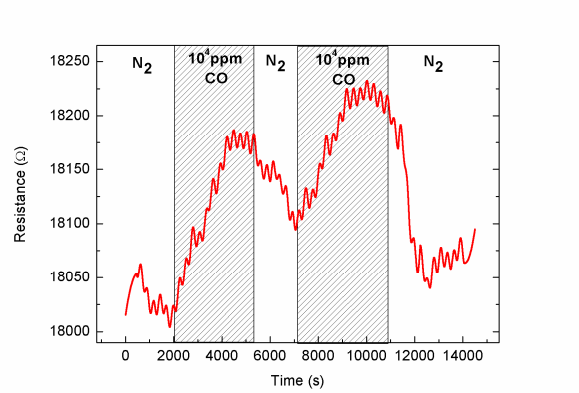

Fig. 9. Sensor resistance under alternating cycles of 10^4 ppm CO and N_2 at 100 °C.

Fig. 8 depicts the static response of the $LaCoO_3$ sensor as a function of operation temperature ranging from 100 to 550 °C for 10^4 ppm CO. The sensor response decrease as the temperature decreases in the temperature range from 150~500 °C. By lowering the temperature, the sensor response decreases rapidly at temperatures above 350 °C, but much slower below 350 °C. To better disclose the sensing property at low temperatures, the region of $T < 260$ °C is magnified in the inset. The sensor still shows reasonable response, for example, a response of ~1.44 can be determined from the static resistance at 100 °C.

To further demonstrate the sensor response to CO at low temperatures, the sensor resistance variation under alternating cycles of 10^4 ppm CO and N_2 at 100 °C was measured and shown in Fig. 9. A response of 1.012 can be obtained from this figure. This is the first time that a reliable dynamic response-and-recovery curve of a $LaCoO_3$-based CO sensor was measured at a temperature as low as 100 °C. Therefore, $LaCoO_3$ is very promising for CO sensing at low temperatures.

In comparison, the resistance of SnO_2 sensors is very high at low temperatures, for example, the electrical conductivity of SnO_2 is about $10^{-4.4}$ to $10^{-3.5}$ S/cm at 100 °C,[31,32] the resistance of ZnO-doped SnO_2 sensors at 300 °C is ~250 MΩ,[33] and the resistance of SnO_2-Co_3O_4 composites thick film sensors at 200 °C is ~3500 MΩ.[34] The very high resistance of SnO_2 sensors makes it impossible to get any reasonable response to CO at temperatures lower than 200 °C.[30,34,35] As for $LaCoO_3$-based sensors, the CO-sensing measurements were mostly carried out at temperatures higher than 150 °C in previous works.[1,36-38] Ghasdi et al. showed the CO response of $LaCoO_3$ as a function of temperature from 100 to 250 °C,[39] and the CO response of $La_{1-x}Ce_xCoO_3$ from 80 to 200 °C.[40] However, the dynamic response-and-recovery curve for CO at 100 °C was not reported in either works.

The oxygen chemisorption and interactions of oxide surface have been extensively investigated;[41-45] it is generally agreed that surfaces are key to the gas sensing performance. Fig. 10 shows the XPS spectra of the La3d, Co2p and O1s levels of $LaCoO_3$. The spectrum of La3d in Fig. 10 (a) is typical of La^{3+}

compounds.[46] It is generally agreed that the double peaks of each spin-orbit split component reflect states with configurations of $\underline{3d}^9 4f^0 L$ and $\underline{3d}^9 4f^1 \underline{L}$,[46] where L denotes the oxygen ligand and underscoring denotes a hole. The spectrum of Co2p (Fig. 10 (b)) shows two main peaks at binding energies of ~780.2 and ~795.3 eV, corresponding to the $Co2p_{3/2}$ and $Co2p_{1/2}$ levels,[2] respectively. The binding energies are close to the values reported in the literature.[47] The XPS spectrum demonstrates that the cobalt is present as trivalent cations. Fig. 10 (c) shows the XPS spectrum of O1s and the deconvolution result. The spectrum presents two strong peaks at ~529.2 and ~531.5 eV. The peak at 529.2 eV can be assigned to the lattice oxygen species O^{2-};[48] whereas the peak at 531.5 eV needs to be deconvoluted into three sub-peaks:[2,49] one at 530.6 eV related to surface-adsorbed oxygen species O_2^{2-}/O^-,[50] one at 531.6 eV due to hydroxyl groups OH^-[51] or possibly carbonate species CO_3^{2-},[52] and one at 532.2 eV due to surface-adsorbed molecular water.[51] The oxygen-containing species might come from the high-temperature calcination of the $LaCoO_3$ nanoparticles and thick films in air. From the relative areas of these sub-peaks, the molar fraction of different oxygen-containing species over the total amount of surface oxygen can be determined, with results listed in Table 1. The ratio between the molar fractions of O_2^{2-}/O^- and OH^-/CO_3^{2-} for the $LaCoO_3$ of this work is much higher than that for conventional $LaCoO_3$, but comparable to that for mesoporous $LaCoO_3$.

As proposed in previous works,[53,54] the oxidation of CO by surface-adsorbed oxygen species O_2^{2-}/O^- is key to the CO-sensing performance. Particularly, the sensing response of $LaCoO_3$ can be represented as follows:[9,37,39]

$$CO_{ads} + O^-_{ads} \rightarrow CO_2 + e^- \quad (4)$$

$$CO_{ads} + 2O^-_{ads} \longleftrightarrow CO_3^{2-} \quad (5)$$

When a CO molecule reacts with adsorbed oxygen, an electron is released. Since $LaCoO_3$ is a *p*-type conductor, the released electrons decrease the hole concentration, thus causing an increase of the sensor resistance. The surface-adsorbed oxygen species, O_2^{2-} and O^-, are important to the CO-sensing performance. In this work, the high content of O_2^{2-} and O^- species on the surface of $LaCoO_3$ may contribute to the high response.

4. Conclusions

$LaCoO_3$ thick film sensors prepared by screen-printing of $LaCoO_3$ nanoparticles demonstrated excellent CO-sensing properties in the temperature range of 100 to 550 °C. A response of 279.86 to 5000 ppm CO was achieved at 500 °C, and a reasonable response of 1.04 to 25 ppm CO was also achieved, demonstrating that the detection limit of the sensor is about 25 ppm. A reliable dynamic response-and-recovery curve was obtained at a temperature as low as 100 °C, and the corresponding response was 1.012. Comparing with the classic CO sensing material of SnO_2, the response of the $LaCoO_3$ sensor is almost one order of magnitude higher, and the $LaCoO_3$ sensor can work effectively at much lower temperatures. The XPS analysis verified that the content of adsorbed oxygen species, O_2^{2-} and O^-, on the surface of $LaCoO_3$ in this work is much higher than those in conventional $LaCoO_3$. The O_2^{2-}/O^- species react with adsorbed CO, causing a change in the sensor resistance; in this way, the high content of O_2^{2-}/O^- species contributes to the high response.

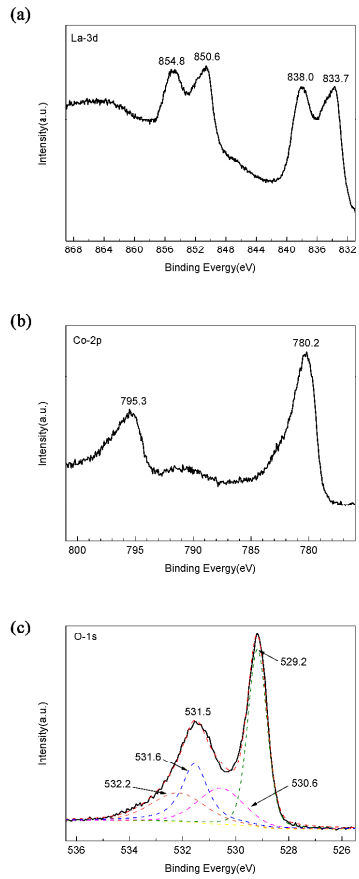

Fig. 10. XPS spectra of $LaCoO_3$: (a) La 3d, (b) Co 2p and (c) O 1s.

Table 1 Deconvolution results of the O1s peak

Samples	O^{2-}(%)	O_2^{2-}/O-(%)	OH^-/CO_3^{2-}(%)	H_2O(%)	$(O_2^{2-}/O^-)/(OH^-/CO_3^{2-})$
$LaCoO_3$ of this work	39.8	19.2	22.9	18.1	0.84
mesoporous $LaCoO_3$[2]	41.5	27.7	27.3	3.5	1.01
conventional $LaCoO_3$[2]	38.0	7.2	42.5	12.3	0.17

Acknowledgements

The analytical and testing center of Huazhong University of Science and Technology is acknowledged for the XPS investigation.

Notes and references

1 A. V. Salker, N. J. Choi, J. H. Kwak, B. S. Joo and D. D. Lee, *Sens. Actuators, B,* 2005, **106**, 461-467.
2 Y. Wang, J. Ren, Y. Wang, F. Zhang, X. Liu, Y. Guo and G. Lu, *J. Phys. Chem. C*, 2008, **112**, 15293-15298.
3 S. Zheng, Q. Hua, W. Gu and B. Liu, *J. Mol. Catal., A*, 2014, **391**, 7-11.
4 L. Zhong, F. Hai, P. Xiao, J. Hong and J. Zhu, *RSC Adv.*, 2014, **4**, 61476-61481.
5 L. Simonot, F. O. Garin and G. Maire, *Appl. Catal., B,* 1997, **11**, 167-179.
6 S. Royer and D. Duprez, *ChemCatChem*, 2011, **3**, 24-65.
7 V. V. Kharton, F. M. Figueiredo, A. V. Kovalevsky, A. P. Viskup, E. N. Naumovich, A. A. Yaremchenko, I. A. Bashmakov and F. Marques, *J. Eur. Ceram. Soc.*, 2001, **21**, 2301-2309.
8 M. A. Señarı´s-Rodrı´guez and J. B. Goodenough, *J. Solid State Chem.*, 1995, **116**, 224-231.
9 J. Ding, H. Li and X. Guo, *Solid State Ionics*, 2015, **272**, 155-159.
10 C. Zhou, Z. Feng, Y. Zhang, L. Hu, R. Chen, B. Shan, H. Yin, W. G. Wang and A. Huang, *RSC Adv.*, 2015, **5**, 28054-28059.
11 J. Chandradass, H. Kim and F. W. Y. Momade, *Adv. Powder Technol.*, 2014, **25**, 1834-1838.
12 D. Singh, N. Choudhary, A. Mahajan, S. Singh and S. Sharma, *Ionics*, 2015, **21**, 1031-1037.
13 S. Lee, J. Lee, Y. Park, J. Wee and K. Lee, *Catal. Today*, 2006, **117**, 376-381.
14 G. Chiarello, J. Grunwaldt, D. Ferri, F. Krumeich, C. Oliva, L. Forni and A. Baiker, *J. Catal.*, 2007, **252**, 127-136.
15 J. W. Zhu, X. J. Sun, Y. P. Wang, X. Wang, X. J. Yang and L. D. Lu, *J. Rare Earth.*, 2007, **25**, 601-604.
16 S. Habibzadeh, A. A. Khodadadi and Y. Mortazavi, *Sens. Actuators, B,* 2010, **144**, 131-138.
17 X. Liu, J. Cui, J. Sun and X. Zhang, *RSC Adv.*, 2014, **4**, 22601-22605.
18 J. He, C. Niu, C. Yang, J. Wang and X. Su, *RSC Adv.*, 2014, **4**, 60253-60259.
19 W. Yan, M. Hu, P. Zeng, S. Ma and M. Li, *Appl. Surf. Sci.*, 2014, **292**, 551-555.
20 S. Mikhaylov, N. Ogurtsov, Y. Noskov, N. Redon, P. Coddeville, J. L. Wojkiewicz and A. Pud, *RSC Adv.*, 2015, **5**, 20218-20226.
21 I. J. Kim, S. D. Han, I. Singh, H. D. Lee and J. S. Wang, *Sens. Actuators, B,* **107**, 825-830.
22 A. Ishikawa, J. Nohara and S. Sugai, *Phys. Rev. Lett.*, 2004, **93,** 136401.
23 C. Tang, C. Wang and S. Chien, *Thermochim. Acta*, 2008, **473**, 68-73.
24 N. Orlovskaya, D. Steinmetz, S. Yarmolenko, D. Pai, J. Sankar and J. Goodenough, *Phys. Rev. B*, 2005, **72,** 014122.
25 M. N. Iliev, M. V. Abrashev, H. G. Lee, V. N. Popov, Y. Y. Sun, C. Thomsen, R. L. Meng and C. W. Chu, *Phys. Rev. B*, 1998, **57**, 2872-2877.
26 M. M. Seikeh, L. Sudheendra, C. Narayana and C. Rao, *J. Mol. Struct.*, 2004, **706**, 121-126.
27 X. Li, Z. Peng, W. Fan, K. Guo, J. Gu, M. Zhao and J. Meng, *Mater. Chem. Phys.*, 1996, **46**, 50-54.
28 S. Durrani, E. E. Khawaja and M. F. Al-Kuhaili, *Talanta*, 2005, **65**, 1162-1167.
29 J. Gerblinger, M. Hausner and H. Meixner, *J. Am. Ceram. Soc.*, 1995, **78**, 1451-1456.
30 Z. A. Ansari, T. G. Ko and J. H. Oh, IEEE Sens. J., 2005, **5**, 817-824.
31 W. J. Moon, J. H. Yu and G. M. Choi, *Sens. Actuators, B,* 2002, **87**, 464-470.
32 J. H. Yu and G. M. Choi, *Sens. Actuators, B,* 1998, **52**, 251-256.
33 E. Nikan, A. A. Khodadadi and Y. Mortazavi, *Sens. Actuators, B,* 2013, **184**, 196-204.
34 U. S. Choi, G. Sakai, K. Shimanoe and N. Yamazoe, *Sens. Actuators, B,* 2004, **98**, 166-173.
35 W. G. Chen, Q. Zhou and S. D. Peng, *Adv. Mater. Sci. Eng.*, 2013, 578460.
36 C. M. Chiu and Y. H. Chang, *Thin Solid Films*, 1999, **342**, 15-19.
37 C. M. Chiu and Y. H. Chang, *Mater. Sci. Eng., A*, 1999, **266**, 93-98.
38 Y. L. Chai, D. T. Ray, H. S. Liu, C. F. Dai and Y. H. Chang, *Mater. Sci. Eng., A*, 2000, **293**, 39-45.
39 M. Ghasdi and H. Alamdari, *Sens. Actuators, B,* 2010, **148**, 478-485.
40 M. Ghasdi, H. Alamdari, S. Royer and A. Adnot, *Sens. Actuators, B,* **156**, 147-155.
41 G. J. Li and S. Kawi, *Mater. Lett.*, 1998, **34**, 99-102.
42 J. F. Xiong, P. Xiao, Q. Wu, X. Z. Wang and Z. Hu, *Acta Chim. Sinica*, 2014, **72**, 433-439.
43 S. Lenaerts, J. Roggen and G. Maes, *Spectrochim. Acta A*, 1995, **51**, 883-894.
44 N. Yamazoe, J. Fuchigami, M. Kishikawa and T. Seiyama, *Surf Sci*, 1979, **86**, 335-344.
45 Chang S C. *J. Vac. Sci. Technol*, 1980, **17**, 366-369.
46 R. P. Vasquez, *Phys. Rev. B*, 1996, **54**, 14938-14941.
47 Y. Wen, C. Zhang, H. He, Y. Yu and Y. Teraoka, *Catal. Today*, 2007, **126**, 400-405.
48 A. Machocki, T. Ioannides, B. Stasinska, W. Gac, G. Avgouropoulos, D. Delimaris, W. Grzegorczyk and S. Pasieczna, *J. Catal.*, 2004, **227**, 282-296.
49 N. A. Merino, B. P. Barbero, P. Eloy and L. E. Cadus, *Appl. Surf. Sci.*, 2006, **253**, 1489-1493.
50 N. Yamazoe, Y. Teraoka and T. Seiyama, *Chem. Lett.*, 1981, **10**, 1767-1770.
51 J. L. G. Fierro, *Catal. Today*, 1990, **8**, 153-174.
52 T. H. Fleisch, R. F. Hicks and A. T. Bell, *J. Catal.*, 1984, **87**, 398-413.
53 O. Lupan, L. Chow, T. Pauporté, L. K. Ono, B. Roldan Cuenya and G. Chai, *Sens. Actuators, B,* 2012, **173**, 772-780.
54 Brosha E L, Mukundan R, Brown D R, Garzon F H, Visser J H, Zanini M, Zhou Z and Logothetis E M. *Sens. Actuators, B,* 2000, **69**, 171-182.